

CHAPTER IV

Sequential solvation of HCl in argon: high resolution infrared spectroscopy of Ar_nHCl ($n = 1,2,3$)

4.1 Introduction

The idea that the properties of condensed matter are ultimately determined by the cumulative pairwise and nonpairwise forces between the constituent molecules or atoms is a powerfully appealing intuitive picture. Though difficult to achieve in practice, this simple picture is at the heart of any theory of macroscopic solvation phenomena in both cluster and condensed phases. Indeed, one long-standing experimental challenge in the cluster community has been to develop detailed spectroscopic methods that can isolate and probe these intermolecular interactions as a function of size, starting first with simple pairs and sequentially adding molecules until the macroscopic limit is eventually reached.^{1,2} Though the field is still far from achieving this limit, a tremendous amount of detailed information about intermolecular forces between pairs of molecules has been obtained by high resolution spectroscopic studies of dimers. When combined with modern quantum theoretical methods, such spectroscopic studies have emerged as an extremely

powerful tool for characterizing true pairwise interactions and have resulted in quantitatively accurate potentials for several systems such as Ar-HCl,³ Ar-HF,⁴ Ar-H₂,⁵ Ar-H₂O,⁶ and Ar-NH₃.⁷

The clear interest in much larger clusters raises new and challenging issues of many body intermolecular contributions to the full potential surface. The basic question can be simply stated; given accurate two-body (i.e., pair) potentials, how well are the interactions of larger ensembles of molecules described by a sum over all possible pairwise interactions? Since an essential prerequisite to addressing this issue rigorously is a quantitatively reliable pair potential, this has been a difficult question to pose, both experimentally and theoretically. Furthermore, the extent to which this “pairwise additive” approximation adequately describes intermolecular forces in clusters varies considerably from system to system; consequently, a study of multiple systems may be necessary to elucidate the correct features of the nonpairwise additive contributions. One clear goal of such studies has been to develop the ability to modify pair potentials by sums over the necessary n-body terms, and thereby provide access to accurate potential energy surfaces for describing arbitrarily large clusters up to and including the condensed phase limit. Though the full fruition of such efforts remains in the future, there have recently been important successes in model systems that indicate significant progress along this path.

One prototypic system that has been particularly revealing for both spectroscopic characterization and theoretical modeling of multibody forces are the

complexes formed between a single hydrogen halide and multiple rare gas Ar atoms. From an experimental standpoint, early microwave experiments by Gutowsky and co-workers on the $\text{Ar}_n\text{HF/DF}$ ($n = 1-4$)⁸⁻¹² and $\text{Ar}_n\text{HCL/DCL}$ ($n = 1-3$)^{13,14} oligomers clearly demonstrated how such a series of cluster sizes could be “synthesized” under supersonic jet conditions and studied in considerable spectroscopic detail. Specifically, these microwave experiments provided information with which to characterize vibrationally averaged structures for each cluster in the series. Far-IR spectroscopic studies by Elrod *et al.* extended this to vibrationally excited levels, characterizing three intermolecular bending state for Ar_2HCl ¹⁵⁻¹⁷ and one in Ar_2DCl .¹⁸ Analogous studies of in-plane and out-of-plane bending states in $\text{Ar}_2\text{HF/DF}$ have recently been conducted via inter- + intra-molecular combination band excitation by Farrell and Nesbitt in the near-IR.¹⁹ Both the near- and far-infrared studies are particularly valuable since direct excitation of the “soft” intermolecular modes provides access to substantially larger regions of the anisotropic angular-radial intermolecular potential. In addition, both Ar_nHF ($n = 1-4$)²⁰ and Ar_nDF ($n = 1-3$)²¹ have been studied in the near-IR via excitation of the intramolecular $\nu_{\text{HX/DX}} = 1$ stretch. Of special importance to the present work, these studies also determined the “red-shift” in the HX vibrational frequency induced by complex formation, which is sensitive to the number of vibrationally averaged structures of the “solvent” Ar atoms.

The Ar_nHX complexes are also particularly accessible from the standpoint of

rigorous theoretical calculations. The Ar-Ar pair potential has been the benchmark atom-atom potential for over 30 years, with the most recent and highly accurate versions determined from a combination of crossed beam scattering and UV spectroscopic studies.²² Arguably the most accurate atom-molecule potentials are the Ar-HCl and Ar-HF potentials developed by Hutson and co-workers^{3,4} from inversion of a large body of high resolution ArHX spectroscopic data. Thus, approximate potentials for HCl “solvated” in an arbitrary number of Ar atoms can be constructed simply by summing over all the pairwise interactions. In principle, solving the multidimensional intermolecular quantum mechanics for nuclear motion on this potential provides a rigorously predictive framework for Ar_nHCl complexes at the pairwise additive level, which can therefore be used to probe for nonpairwise additive effects. Indeed, Hutson and co-workers²³ have performed close coupling calculations for Ar₂HCl/DCl that explicitly include all intermolecular coordinates, with the high frequency stretching coordinate included parametrically as a function of ν_{HCl} . A comparison of the rotational constants and vibrational frequencies calculated on the pairwise additive potential have identified significant discrepancies with experiment that are attributable to nonadditive terms in the full potential surface. Several nonadditive contributions have been investigated, from which it was found that additional terms accounting for three-body dispersion, induction, and exchange interactions are necessary to bring the calculated results into good agreement with experiment.

Another experimental observable which can be provided by near-infrared studies of the Ar_nHCl family is the shift in the vibrational frequency of the HCl chromophore. This shift is quite sensitive to the local structure of the Ar atoms around the HCl. High resolution rotationally resolved spectra allow the size of the cluster to be determined unambiguously, which permits the redshift to be studied as a function of the number of Ar atoms in the complex.^{20,21} At the other extreme, the vibrational red-shift can also be determined accurately under rare gas matrix isolation conditions,^{24,25} i.e., effectively in the limit of an infinite number of solvation shells. Vibrational red-shifts in the intermediate size clusters, therefore, potentially offer a quantitative link between the study of dimer and bulk condensed phase phenomena.

In the present work, we employ high resolution infrared absorption spectroscopy to vibrationally excite the HCl moiety in the Ar_2HCl and Ar_3HCl . Analysis of the resulting rotationally resolved spectra allows us to size-select the different clusters formed in a slit jet expansion. For each cluster the rotational constants are used to infer the vibrationally averaged structure in the HCl stretch excited state. These structures can be compared with those determined for the ground intramolecular state from microwave and far-IR spectra to quantify the effect of vibrational excitation of the HCl chromophore. To make a more direct comparison with this experimental data, we also take advantage of the well determined Ar-Ar and Ar-HCl pair potentials to construct a multidimensional

pairwise additive potential for Ar_nHCl clusters. In conjunction with classical energy minimization methods, we theoretically examine the equilibrium structures of much larger Ar_nHCl ($n < 55$) clusters and the vibrational red-shift for HCl embedded in large ensemble lattices of Ar atoms intended to mimic the relevant cage sizes and internal forces in the bulk solid Ar environment.

4.2 Experiment

The Ar_nHCl complexes are formed by adiabatically expanding mixtures of 0.5% HCl in a 50-50 mix of Ar and Ne-70, at a backing pressure of 450 Torr, through a 4 cm x 190 μm pulsed slit jet. The complexes are detected via time-gated, dual beam direct infrared absorption detection. As described in detail in chapter 2, the infrared light is generated via nonlinear mixing of a single mode, fixed frequency Ar^+ laser (514.5 nm) and a single mode, tunable ring dye laser operating on R6G. Multipass optics are used to pass the infrared light 20 times through the expansion for a total absorption path length of 80 cm.

The single frequency Ar^+ laser is frequency stabilized to a transfer cavity that is actively locked to a polarization stabilized HeNe laser. The transmission fringes obtained by scanning the dye laser are also recorded with the transfer cavity to permit the measurement of relative frequencies to a precision better than 0.0001 cm^{-1} . This frequency precision, discussed more thoroughly in chapter 2, proved invaluable for

the assignment and analysis of the spectra of these large Ar_nHCl clusters since this region of the spectrum is heavily congested with strong transitions due to ArHCl (for both the ArH^{35}Cl and ArH^{37}Cl isotopomers) and $(\text{HCl})_2$. Absolute frequency calibration is made with respect to the P(16) transition (2882.3036 cm^{-1}) of the ArH^{35}Cl fundamental.²⁶ This calibration procedure allows the transition frequencies and vibrational origins to be reported to an absolute accuracy of 0.0002 cm^{-1} .

4.3 Results and analysis

4.3.1 Ar_2HCl

Previous analyses by Gutowsky and coworkers in the microwave,¹³ and by Saykally and coworkers in the far-IR¹⁵⁻¹⁷ have inferred that the equilibrium geometry of Ar_2HCl is T-shaped, with the HCl pointing along the C_2 symmetry axis of the complex. The transition moment for excitation of the HCl stretch lies along the a inertial axis, and consequently excitation of the $\nu_{\text{HCl}} = 1 \leftarrow 0$ near-IR fundamental should result in an A-type band with asymmetric top structure and a strong central Q -branch.. In good qualitative agreement with these expectations, there are two features characteristic of an asymmetric top Q -branch, separated by

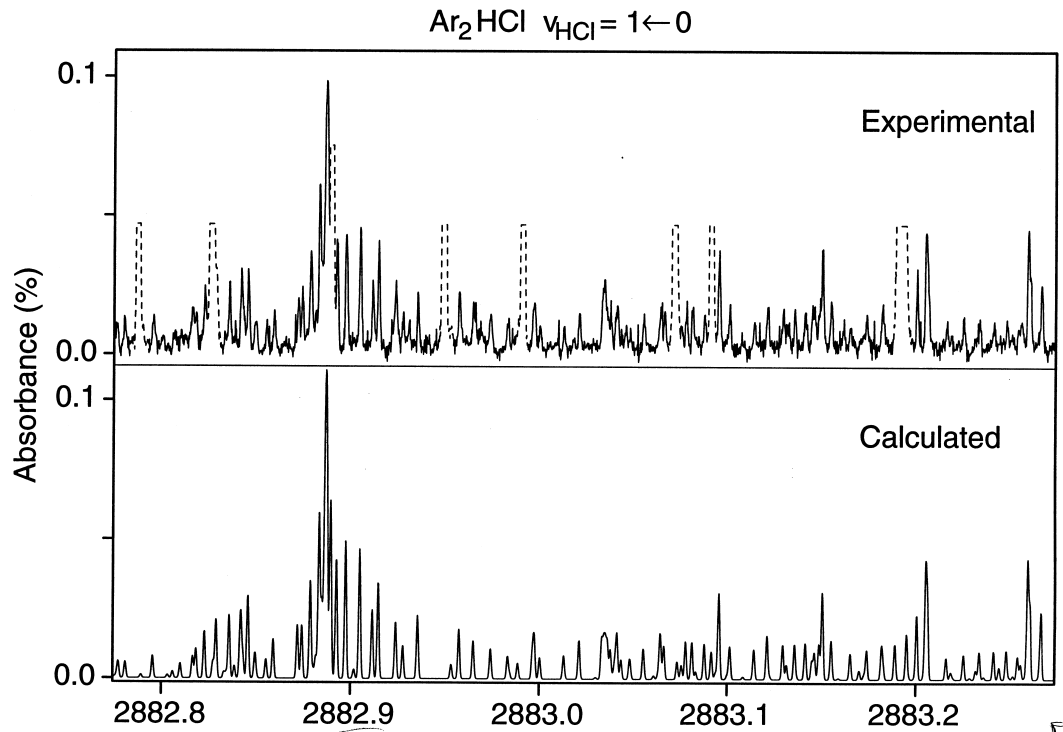


Figure 4.1 Experimental and calculated spectra for $\text{Ar}_2\text{H}^{35}\text{Cl}$ near the band origin. The calculated spectrum is generated using the constants in Table 4.3, obtained from a least squared fit of the experimental data. The dotted line peaks in the experimental spectrum are transitions due to ArH^{35}Cl , ArH^{37}Cl , and $(\text{HCl})_2$, and have been suppressed to highlight the $\text{Ar}_2\text{H}^{35}\text{Cl}$ structure.

approximately 2.1 cm^{-1} with the feature to the blue approximately three times stronger in intensity. The frequency separation and relative intensities of these two features are consistent with the two isotopomers expected for a complex containing a single HCl molecule, with H^{35}Cl and H^{37}Cl present in 3:1 natural abundance.

Figure 4.1 shows a sample 0.5 cm^{-1} scan region around the Q -branch feature assigned to the ArH^{35}Cl isotopomer, demonstrating the exceedingly dense spectral structure due to the trimer species.

The rotational structure for both isotopomers is readily assigned using ground state combination differences calculated from the rotational constants determined by Elrod *et al.*¹⁵ and permits unambiguous labeling of the lower $J_{K_a K_c}$ rotational quantum numbers. This method of assignment takes maximum advantage of the high frequency precision of the spectrometer (~ 5 MHz), which proves essential due to the high density of lines in the spectrum even under 5-10 K slit jet expansion conditions. The root mean square (rms) deviation between observed and calculated combination differences is ≈ 6 MHz, i.e., consistent with the experimental uncertainty. Furthermore, since rotation about the a inertial axis (i.e., the C_2 axis) for the Ar_2HCl complex involves exchange of identical boson nuclei (^{40}Ar ; $I=0$), nuclear spin constraints on the total wave function restrict K_a to even non-negative integers in the ground state. Thus the assignment can be additionally confirmed by the complete absence of transitions out of $K_a = 1, 3, 5, \dots$ lower levels. Infrared selection rules identify this as an A -type band (i.e., $\Delta K_a = 0, \pm 2, \dots$, $\Delta K_c = \pm 1, \pm 3, \dots$), which is consistent with a vibrational transition moment along the $\text{Ar}_2\text{-HCl}$ intermolecular axis. The observed transition frequencies are listed in Tables 4.1 and 4.2. for the $\text{Ar}_2\text{H}^{35}\text{Cl}$ and $\text{Ar}_2\text{H}^{37}\text{Cl}$ isotopomer species, respectively..

The infrared data can be well fit to a S -reduction, III^r representation Watson asymmetric top Hamiltonian.²⁷ All near-IR data are consistent with the previously determined ground state constants,¹⁵ which are therefore held fixed in the spectral fits. Fitted molecular constants for both isotopomers are reported in Table 4.3. The

rms deviation of the $\text{Ar}_2\text{H}^{35}\text{Cl}$ and $\text{Ar}_2\text{H}^{37}\text{Cl}$ fits are 0.00017 and 0.00018 cm^{-1} , respectively, again comparable to or greater than the 0.0001 cm^{-1} experimental precision. A comparison of the experimental data with a simulated spectrum generated using the constants from the fit is shown in Figure 4.1 for $\text{Ar}_2\text{H}^{35}\text{Cl}$, corroborating the assignment and demonstrating the high quality of the fit. The band origin for $\text{Ar}_2\text{H}^{35}\text{Cl}$ is 2882.75176(3) cm^{-1} , i.e., redshifted 3.2236 cm^{-1} from the uncomplexed H^{35}Cl origin and approximately twice as large as the 1.7667 cm^{-1} shift for a single Ar atom in ArHCl .²⁶ The nearly linear dependence of the red-shift on the number of Ar atoms is substantially different from the much more nonlinear n dependence measured^{20,21} for both Ar_nHF and Ar_nDF , i.e., where the incremental red-shift decreases with successive Ar atoms. We will return to the possible reasons for this discrepancy in greater detail in the Discussion.

4.3.2 Ar_3HCl

With the Ar_2HCl transitions satisfactorily assigned, we are in a position to interrogate the much less intense additional features due to larger clusters. Indeed only after all the Ar_2HCl transitions were identified and assigned did an unassigned weak feature at $\sim 2881.45 \text{ cm}^{-1}$ become evident. This feature is shown in Figure 4.2 where at the top of the figure the experimentally measured spectrum is shown. Directly below the experimental spectrum is a model Ar_2HCl spectrum

Table 4.1 Observed transition frequencies for the $\nu_{\text{HCl}} = 1 \leftarrow 0$ transition in $\text{Ar}_2\text{H}^{35}\text{Cl}$.

$J_{K_a, K_c} \leftarrow J_{K_a, K_c}^2$	Wavenumber (cm^{-1})	$J_{K_a, K_c} \leftarrow J_{K_a, K_c}^2$	Wavenumber (cm^{-1})
$21_{0,21} \leftarrow 20_{0,20}$	2883.88856	$8_{2,6} \leftarrow 7_{2,5}$	2883.32821
$20_{0,20} \leftarrow 19_{0,19}$	2883.83885	$10_{0,10} \leftarrow 9_{0,9}$	2883.32564
$11_{8,3} \leftarrow 10_{8,2}$	2883.82230	$7_{2,5} \leftarrow 6_{2,4}$	2883.27556
$12_{8,5} \leftarrow 11_{8,4}$	2883.80746	$6_{4,3} \leftarrow 5_{4,2}$	2883.27556
$13_{6,7} \leftarrow 12_{6,6}$	2883.80353	$9_{0,9} \leftarrow 8_{0,8}$	2883.27257
$14_{6,9} \leftarrow 13_{6,8}$	2883.79983	$5_{4,1} \leftarrow 4_{4,0}$	2883.26052
$19_{0,19} \leftarrow 18_{0,18}$	2883.78858	$12_{4,9} \leftarrow 12_{2,10}$	2883.25713
$13_{6,8} \leftarrow 12_{6,7}$	2883.74966	$13_{4,9} \leftarrow 13_{4,10}$	2883.24847
$14_{4,10} \leftarrow 13_{4,9}$	2883.74645	$6_{2,4} \leftarrow 5_{2,3}$	2883.22179
$15_{4,12} \leftarrow 14_{4,11}$	2883.74363	$8_{0,8} \leftarrow 7_{0,7}$	2883.21903
$16_{2,14} \leftarrow 15_{2,13}$	2883.74140	$5_{4,2} \leftarrow 4_{4,1}$	2883.21421
$18_{0,18} \leftarrow 17_{0,17}$	2883.73905	$11_{4,8} \leftarrow 11_{2,9}$	2883.20515
$12_{6,7} \leftarrow 11_{6,6}$	2883.69927	$12_{4,8} \leftarrow 12_{4,9}$	2883.19678
$14_{4,11} \leftarrow 13_{4,10}$	2883.69332	$5_{2,3} \leftarrow 4_{2,2}$	2883.16899
$17_{0,17} \leftarrow 16_{0,16}$	2883.68843	$9_{2,7} \leftarrow 9_{2,8}$	2883.15942
$16_{2,15} \leftarrow 15_{2,14}$	2883.68843	$10_{4,7} \leftarrow 10_{2,8}$	2883.15254
$10_{6,4} \leftarrow 9_{6,3}$	2883.65410	$11_{4,7} \leftarrow 11_{4,8}$	2883.14482
$11_{6,6} \leftarrow 10_{6,5}$	2883.64834	$4_{2,2} \leftarrow 3_{2,1}$	2883.11826
$11_{4,7} \leftarrow 10_{4,6}$	2883.59389	$6_{0,6} \leftarrow 5_{0,5}$	2883.11122
$12_{4,9} \leftarrow 11_{4,8}$	2883.59110	$15_{8,7} \leftarrow 15_{8,8}$	2883.10750
$8_{6,2} \leftarrow 7_{6,1}$	2883.55065	$9_{4,6} \leftarrow 9_{2,7}$	2883.09972
$9_{6,4} \leftarrow 8_{6,3}$	2883.54534	$4_{0,4} \leftarrow 3_{0,3}$	2883.00181
$10_{4,6} \leftarrow 9_{4,5}$	2883.54242	$7_{4,4} \leftarrow 7_{2,5}$	2882.99282
$11_{4,8} \leftarrow 10_{4,7}$	2883.53967	$8_{4,4} \leftarrow 8_{4,5}$	2882.98728
$12_{2,10} \leftarrow 11_{2,9}$	2883.53735	$9_{6,4} \leftarrow 9_{4,5}$	2882.98116
$14_{0,14} \leftarrow 13_{0,13}$	2883.53476	$10_{6,4} \leftarrow 10_{6,5}$	2882.97285
$13_{2,12} \leftarrow 12_{2,11}$	2883.53476	$11_{8,4} \leftarrow 11_{6,5}$	2882.96574
$9_{4,5} \leftarrow 8_{4,4}$	2883.49043	$3_{0,3} \leftarrow 2_{0,2}$	2882.94700
$10_{4,7} \leftarrow 9_{4,6}$	2883.48795	$2_{0,2} \leftarrow 1_{0,1}$	2882.89264
$11_{2,9} \leftarrow 10_{2,8}$	2883.48557	$1_{0,1} \leftarrow 0_{0,0}$	2882.83482
$13_{0,13} \leftarrow 12_{0,12}$	2883.48310	$0_{0,0} \leftarrow 1_{0,1}$	2882.66752
$6_{6,0} \leftarrow 5_{4,1}$	2883.47695	$3_{0,3} \leftarrow 4_{0,4}$	2882.49566
$7_{6,1} \leftarrow 6_{6,0}$	2883.45982	$2_{2,0} \leftarrow 3_{2,1}$	2882.44502
$8_{4,4} \leftarrow 7_{4,3}$	2883.43956	$4_{0,4} \leftarrow 5_{0,5}$	2882.43806
$9_{4,6} \leftarrow 8_{4,5}$	2883.43598	$5_{0,5} \leftarrow 6_{0,6}$	2882.38001
$10_{2,8} \leftarrow 9_{2,7}$	2883.43356	$3_{2,1} \leftarrow 4_{2,2}$	2882.37411
$12_{0,12} \leftarrow 11_{0,11}$	2883.43107	$6_{0,6} \leftarrow 7_{0,7}$	2882.32171
$7_{4,3} \leftarrow 6_{4,2}$	2883.38986	$4_{2,2} \leftarrow 5_{2,3}$	2882.32171
$8_{4,5} \leftarrow 7_{4,4}$	2883.38336	$4_{4,1} \leftarrow 5_{4,2}$	2882.27882
$9_{2,7} \leftarrow 8_{2,6}$	2883.38089	$7_{0,7} \leftarrow 8_{0,8}$	2882.26305
$11_{0,11} \leftarrow 10_{0,10}$	2883.37838	$5_{2,3} \leftarrow 6_{2,4}$	2882.26315
$6_{4,2} \leftarrow 5_{4,1}$	2883.33892	$4_{4,0} \leftarrow 5_{4,1}$	2882.22618

Table 4.1 continued

$J_{K_a, K_c} \leftarrow J_{K_a, K_c}^2$	Wavenumber (cm ⁻¹)	$J_{K_a, K_c} \leftarrow J_{K_a, K_c}^2$	Wavenumber (cm ⁻¹)
5 _{4,2} ← 6 _{4,3}	2882.20807	11 _{6,6} ← 11 _{4,7}	2883.08540
8 _{0,8} ← 9 _{0,9}	2882.20443	12 _{6,6} ← 12 _{6,7}	2883.07678
6 _{2,4} ← 7 _{2,5}	2882.20443	13 _{8,6} ← 13 _{6,7}	2883.06781
9 _{0,9} ← 10 _{0,10}	2882.14539	5 _{0,5} ← 4 _{0,4}	2883.05687
7 _{2,5} ← 8 _{2,6}	2882.14539	3 _{2,1} ← 2 _{2,0}	2883.05191
5 _{4,1} ← 6 _{4,2}	2882.13694	10 _{6,5} ← 10 _{4,6}	2883.03372
10 _{0,10} ← 11 _{0,11}	2882.08593	11 _{6,5} ← 11 _{6,6}	2883.02530
8 _{2,6} ← 9 _{2,7}	2882.08593	13 _{8,5} ← 13 _{8,6}	2883.00660
6 _{4,2} ← 7 _{4,3}	2882.08106	19 _{2,17} ← 20 _{2,18}	2881.41430
6 _{6,1} ← 7 _{6,2}	2882.06184	22 _{0,22} ← 23 _{0,23}	2881.35174
11 _{0,11} ← 12 _{0,12}	2882.02633	20 _{2,18} ← 21 _{2,19}	2881.35174
9 _{2,7} ← 10 _{2,8}	2882.02633	23 _{0,23} ← 24 _{0,24}	2881.28881
8 _{4,5} ← 9 _{4,6}	2882.02633	24 _{0,24} ← 25 _{0,25}	2881.22577
7 _{4,3} ← 8 _{4,4}	2882.02633	25 _{0,25} ← 26 _{0,26}	2881.16231
6 _{6,0} ← 7 _{6,1}	2882.01435	26 _{0,26} ← 27 _{0,27}	2881.09878
7 _{6,2} ← 8 _{6,3}	2881.97845		
12 _{0,12} ← 13 _{0,13}	2881.96641		
10 _{2,8} ← 11 _{2,9}	2881.96641		
8 _{6,3} ← 9 _{6,4}	2881.91124		
9 _{4,5} ← 10 _{4,6}	2881.90851		
13 _{0,13} ← 14 _{0,14}	2881.90619		
11 _{2,9} ← 12 _{2,10}	2881.90619		
7 _{6,1} ← 8 _{6,2}	2881.90190		
10 _{4,6} ← 11 _{4,7}	2881.84827		
14 _{0,14} ← 15 _{0,15}	2881.84567		
12 _{2,10} ← 13 _{2,11}	2881.84567		
6 _{6,2} ← 9 _{6,3}	2881.83520		
11 _{4,7} ← 12 _{4,8}	2881.78749		
15 _{0,15} ← 16 _{0,16}	2881.78462		
13 _{2,11} ← 14 _{2,12}	2881.78462		
16 _{0,16} ← 17 _{0,17}	2881.72302		
14 _{2,12} ← 15 _{2,13}	2881.72302		
17 _{0,17} ← 18 _{0,18}	2881.66234		
15 _{2,13} ← 16 _{2,14}	2881.66234		
18 _{0,18} ← 19 _{0,19}	2881.60065		
16 _{2,14} ← 17 _{2,15}	2881.60065		
19 _{0,19} ← 20 _{0,20}	2881.53889		
17 _{2,15} ← 18 _{2,16}	2881.53889		
20 _{0,20} ← 21 _{0,21}	2881.47682		
18 _{2,16} ← 19 _{2,17}	2881.47682		
21 _{0,21} ← 22 _{0,22}	2881.41430		
10 _{4,6} ← 10 _{4,7}	2883.09288		

Table 4.2 Observed transition frequencies for the $\nu_{\text{HCl}}=1\leftarrow 0$ transition in $\text{Ar}_2\text{H}^{37}\text{Cl}$.

$J_{K^a,K^c} \leftarrow J_{K^a,K^c}^2$	Wavenumber (cm^{-1})	$J_{K^a,K^c} \leftarrow J_{K^a,K^c}^2$	Wavenumber (cm^{-1})
23 _{0,23} \leftarrow 22 _{0,22}	2881.87076	4 _{4,0} \leftarrow 4 _{4,1}	2880.66986
19 _{0,19} \leftarrow 18 _{0,18}	2881.67717	6 _{6,0} \leftarrow 6 _{6,1}	2880.66110
18 _{0,18} \leftarrow 17 _{0,17}	2881.62813	8 _{8,0} \leftarrow 8 _{8,1}	2880.65639
17 _{0,17} \leftarrow 16 _{0,16}	2881.57888	4 _{4,1} \leftarrow 4 _{4,0}	2880.64620
10 _{8,3} \leftarrow 9 _{8,2}	2881.56821	2 _{2,1} \leftarrow 2 _{2,0}	2880.63812
16 _{0,16} \leftarrow 15 _{0,15}	2881.52892	13 _{12,1} \leftarrow 13 _{12,2}	2880.62968
9 _{6,3} \leftarrow 8 _{6,2}	2881.50446	2 _{0,2} \leftarrow 3 _{0,3}	2880.46574
9 _{8,1} \leftarrow 8 _{8,0}	2881.49842	8 _{4,4} \leftarrow 6 _{6,3}	2880.44350
10 _{6,5} \leftarrow 9 _{6,4}	2881.48902	10 _{6,4} \leftarrow 10 _{8,3}	2880.41905
13 _{0,13} \leftarrow 12 _{0,12}	2881.37781	2 _{2,1} \leftarrow 3 _{2,2}	2880.41676
8 _{4,4} \leftarrow 7 _{4,3}	2881.33759	3 _{0,3} \leftarrow 4 _{0,4}	2880.40955
9 _{4,6} \leftarrow 8 _{4,5}	2881.33140	6 _{2,5} \leftarrow 6 _{2,4}	2880.40125
7 _{4,3} \leftarrow 6 _{4,2}	2881.29227	7 _{2,5} \leftarrow 7 _{4,4}	2880.39729
8 _{4,5} \leftarrow 7 _{4,4}	2881.27955	8 _{4,5} \leftarrow 8 _{4,4}	2880.39435
6 _{4,2} \leftarrow 5 _{4,1}	2881.23201	10 _{6,5} \leftarrow 10 _{6,4}	2880.38748
7 _{2,5} \leftarrow 6 _{2,4}	2881.17434	11 _{6,5} \leftarrow 11 _{8,4}	2880.37390
9 _{0,9} \leftarrow 8 _{0,8}	2881.17144	2 _{2,0} \leftarrow 3 _{2,1}	2880.36579
8 _{0,8} \leftarrow 7 _{0,7}	2881.11923	4 _{0,4} \leftarrow 5 _{0,5}	2880.35328
5 _{2,3} \leftarrow 4 _{2,2}	2881.07184	5 _{0,5} \leftarrow 6 _{0,6}	2880.29597
7 _{0,7} \leftarrow 6 _{0,6}	2881.06649	3 _{2,1} \leftarrow 4 _{2,2}	2880.28877
4 _{2,2} \leftarrow 3 _{2,1}	2881.02156	6 _{0,6} \leftarrow 7 _{0,7}	2880.23883
6 _{0,6} \leftarrow 5 _{0,5}	2881.01337	4 _{2,2} \leftarrow 5 _{2,3}	2880.23425
9 _{4,6} \leftarrow 9 _{2,7}	2881.00109	7 _{0,7} \leftarrow 8 _{0,8}	2880.18151
5 _{0,5} \leftarrow 4 _{0,4}	2880.95999	6 _{2,5} \leftarrow 7 _{2,6}	2880.18151
7 _{2,5} \leftarrow 7 _{2,6}	2880.95453	5 _{2,3} \leftarrow 6 _{2,4}	2880.18151
8 _{4,5} \leftarrow 8 _{2,6}	2880.94902	5 _{4,2} \leftarrow 6 _{4,3}	2880.13169
9 _{4,5} \leftarrow 9 _{4,6}	2880.94125	8 _{0,8} \leftarrow 9 _{0,9}	2880.12362
4 _{0,4} \leftarrow 3 _{0,3}	2880.90629	6 _{4,3} \leftarrow 7 _{4,4}	2880.06746
6 _{2,4} \leftarrow 6 _{2,5}	2880.90140	9 _{0,9} \leftarrow 10 _{0,10}	2880.06562
7 _{4,4} \leftarrow 7 _{2,5}	2881.89638	5 _{4,1} \leftarrow 6 _{4,2}	2880.06160
6 _{6,4} \leftarrow 9 _{4,5}	2881.88301	10 _{0,10} \leftarrow 11 _{0,11}	2880.00737
6 _{4,3} \leftarrow 6 _{2,4}	2881.84157	6 _{4,2} \leftarrow 7 _{4,3}	2879.99471
8 _{6,3} \leftarrow 8 _{4,4}	2880.83676	6 _{6,0} \leftarrow 7 _{6,1}	2879.97457
7 _{4,3} \leftarrow 7 _{4,4}	2880.83094	11 _{0,11} \leftarrow 12 _{0,12}	2879.94883
2 _{0,2} \leftarrow 1 _{0,1}	2880.79940	12 _{2,9} \leftarrow 11 _{2,10}	2879.94883
4 _{2,2} \leftarrow 4 _{2,3}	2880.78915	9 _{2,7} \leftarrow 10 _{2,8}	2879.94883
2 _{2,1} \leftarrow 2 _{0,2}	2880.75132	7 _{4,3} \leftarrow 8 _{4,4}	2879.94462
8 _{6,2} \leftarrow 8 _{6,3}	2880.72800	12 _{0,12} \leftarrow 13 _{0,13}	2879.89002
3 _{2,1} \leftarrow 3 _{2,2}	2880.72800	11 _{2,0} \leftarrow 12 _{2,11}	2879.89002
5 _{4,1} \leftarrow 5 _{4,2}	2880.70470	10 _{2,8} \leftarrow 11 _{2,9}	2879.89002
2 _{2,0} \leftarrow 2 _{2,1}	2880.68169	7 _{6,1} \leftarrow 8 _{6,2}	2879.84676
7 _{6,1} \leftarrow 7 _{6,2}	2880.67758	8 _{6,3} \leftarrow 9 _{6,4}	2879.83912

Table 4.2 continued.

$J\zeta_{K_a, K_c} \leftarrow J^2_{K^2_a, K^2_c}$	Wavenumber (cm ⁻¹)	$J\zeta_{K_a, K_c} \leftarrow J^2_{K^2_a, K^2_c}$	Wavenumber (cm ⁻¹)
13 _{0,13} ← 14 _{0,14}	2879.83071	18 _{0,18} ← 19 _{0,19}	2879.53056
14 _{0,14} ← 15 _{0,15}	2879.77119	10 _{8,2} ← 11 _{8,3}	2879.52495
15 _{0,15} ← 16 _{0,16}	2879.77154	19 _{0,19} ← 20 _{0,20}	2879.46969
9 _{8,2} ← 10 _{8,3}	2879.70319	20 _{0,20} ← 21 _{0,21}	2879.48021
10 _{8,3} ← 11 _{8,4}	2879.61359	19 _{2,18} ← 20 _{22,19}	2879.40821
17 _{0,17} ← 18 _{0,18}	2879.59131	12 _{10,3} ← 13 _{10,4}	2879.39432

Table 4.3 Spectroscopic constants (in cm⁻¹) determined from fits of the transition frequencies to an *S*-reduction Watson Hamiltonian using the III^f representation. The $\nu_{\text{HCl}} = 0$ ground state values were fixed at values determined from microwave and far-IR studies.^{a,b} The uncertainties in parentheses represent one standard deviation in the units of the last reported digit.

	Ar ₂ H ³⁵ Cl		Ar ₂ H ³⁷ Cl	
	$\nu_{\text{HCl}} = 0$	$\nu_{\text{HCl}} = 1$	$\nu_{\text{HCl}} = 0$	$\nu_{\text{HCl}} = 1$
A	0.0578835211(13)	0.0578417(16)	0.057834167(13)	0.05785902(33)
B	0.055635869(6)	0.0550508(17)	0.05359925(17)	0.0530277(43)
C	0.028167649(5)	0.02801808(37)	0.027634232(5)	0.02748511(57)
$D_J \times 10^5$	0.080726(23)	0.08015(37)	0.07795(5)	0.0858(18)
$D_{JK} \times 10^5$	-0.13648(6)	-0.1340(9)	-0.13119(5)	-0.14173(40)
$D_K \times 10^5$	0.062306(47)	0.06041(63)	0.06041(63)	0.0622(23)
$d_1 \times 10^5$	-0.008269(20)	-0.00891(40)	-0.009763(3)	-0.0203(16)
$d_2 \times 10^5$	-0.001356(6)	-0.0057(37)	-0.001521(3)	-0.005(10)
ν_0	2882.75176(3)		2880.66089(5)(3)	

^a Reference 13

^b Reference 15-17

generated from the constants in Table 4.3. Since in this region of the spectrum transitions due to both $\text{Ar}_2\text{H}^{35}\text{Cl}$ and $\text{Ar}_2\text{H}^{37}\text{Cl}$ are present, the model spectrum is a summation of the spectra for both isotopomers weighted by the 3:1 natural abundance of $^{35}\text{Cl}:^{37}\text{Cl}$. After subtracting the calculated spectrum from the experimental data (in addition three relatively strong features due to ArH^{37}Cl , ArH^{35}Cl , and $(\text{HCl})_2$ in this region are also subtracted), the unaccounted for feature at 2881.46 cm^{-1} becomes more apparent (see Figure 4.2). Indeed a similar type of analysis throughout the spectrum convincingly displays the excellent modeling of the Ar_2HCl features that enable their contribution to the observed spectrum to be effectively extracted.

Based on the previous microwave studies of Gutwosky et al.,¹⁴ the equilibrium geometry of the Ar_3HCl tetramer has C_{3v} symmetry, with the HCl pointing along the C_3 symmetry axis. The HCl monomer lies along the symmetric top axis indicating that the near-IR $\nu_{\text{HCl}} = 1 \leftarrow 0$ fundamental should be a parallel band ($\Delta K=0$). The three equivalent Ar atoms with nuclear spin $I = 0$ limits the available quantum states by Bose-Einstein statistics, such that only $K = 0, \pm 3, \pm 6 \dots$ states have non-zero statistical weights in the ground vibrational state. The unassigned feature is characteristic of the central Q -branch of a symmetric top, and thus used as a guide for a search for additional P/R transitions. Using $\text{Ar}_3\text{H}^{35}\text{Cl}$ combination differences calculated from the microwave molecular constants, nearly perfectly overlapping $K = 0, \pm 3$ transitions in the P/R -branch were assigned centered around the suspected Q -

Extracting the $\text{Ar}_3\text{H}^{35}\text{Cl}$ Q-branch Signal

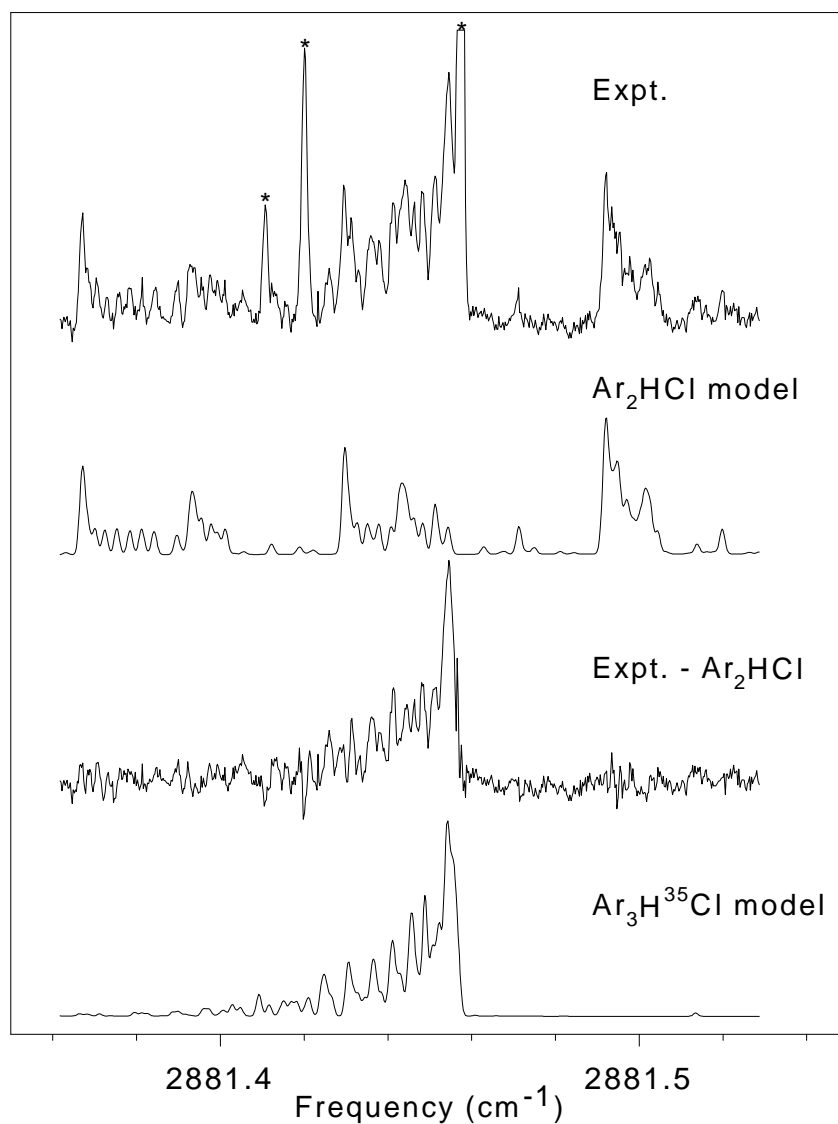


Figure 4.2 Sample data indicating how Ar_3HCl and Ar_2HCl cluster spectra can be extracted separately. (a) The experimentally observed spectrum near the $\text{Ar}_3\text{H}^{35}\text{Cl}$ Q-branch region. (b) A least squares fit of the full Ar_2HCl spectrum in this region, which is a sum of the calculated spectra for both the $\text{Ar}_2\text{H}^{35}\text{Cl}$ and $\text{Ar}_2\text{H}^{37}\text{Cl}$ complexes weighted by the 3:1 $^{35}\text{Cl}:$ ^{37}Cl natural abundance ratio. (c) The contribution of just the Ar_3HCl clusters obtained by subtracting the Ar_2HCl model from the experimental spectrum [i.e., (a) - (b)]. (d) A least squares fit of the residual $\text{Ar}_3\text{H}^{37}\text{Cl}$ spectrum. The peaks marked with asterisks in (a) are due to contaminating ArHCl and $(\text{HCl})_2$ species and have been subtracted in (b), (c), and (d).

branch feature. Even higher K states could also be assigned using ground state combination differences for approximately 10 transitions. The P/R -branch structure is fit to a symmetric top Hamiltonian,

$$E = BJ(J+1) + (A-B)K^2 - D_JJ(J+1)^2 - D_{JK}J(J+1)K^2 - D_KK^4 \quad (4.1)$$

with the ground state constants held fixed. Due to the parallel nature of the transitions ($\Delta K=0$), only the upper state B , D_J , and D_{JK} molecular constants can be determined uniquely. Therefore, the upper state B , D_J , and D_{JK} constants are determined from a fit where ΔA and ΔD_K are fixed at zero, as listed in Table 4.5. However, further information on ΔA and ΔD_K for the Ar_3HCl cluster can be obtained from least squares modelling of the Q -branch structure; these values are also reported in Table 4.5. The final simulation using all the fitted parameters is presented in Figure 4.2 and demonstrates that the shading and relative intensity of the Q -branch is well reproduced.

Further corroboration of the above $\text{Ar}_3\text{H}^{35}\text{Cl}$ assignment is obtained by identifying the corresponding $\text{Ar}_3\text{H}^{37}\text{Cl}$ band. Based on the a S/N ratio of 10 on the $\text{Ar}_3\text{H}^{35}\text{Cl}$ Q -branch, the corresponding Q -branch feature for $\text{Ar}_3\text{H}^{37}\text{Cl}$ is expected approximately 2 cm^{-1} to the red with a S/N ratio of ~ 3 . Indeed, a small feature with the correct relative intensity at 2.1 cm^{-1} to the red of the feature assigned to $\text{Ar}_3\text{H}^{35}\text{Cl}$ is observed but since the corresponding P/R-branch transitions are weaker still, a

Table 4.4 Observed transition frequencies for the $\nu_{\text{HCl}} = 1 \leftarrow 0$ transition in $\text{Ar}_3\text{H}^{35}\text{Cl}$.

$J_{K_c} \leftarrow J_{K^z}$	Wavenumber (o-c)	$J_{K_c} \leftarrow J_{K^z}$	Wavenumber (o-c)
$18_0 \leftarrow 17_0$	2882.40055(0)	$4_0 \leftarrow 5_0$	2881.15767(1)
$17_0 \leftarrow 16_0$	2882.35009(-2)	$5_0 \leftarrow 6_0$	2881.09992(1)
$16_0 \leftarrow 15_0$	2882.29947(-1)	$6_6 \leftarrow 7_6$	2881.04750(13) ^b
$15_9 \leftarrow 14_9$	2882.25949(17) ^b	$6_3 \leftarrow 7_3$	2881.04421(14) ^b
$15_6 \leftarrow 14_6$	2882.25267(1)	$6_0 \leftarrow 7_0$	2881.04132(-4) ^b
$15_0 \leftarrow 14_0$	2882.24849(0)	$7_6 \leftarrow 8_6$	2880.98784(0)
$14_6 \leftarrow 13_6$	2882.20127(0)	$7_0 \leftarrow 8_0$	2880.98348(2)
$14_0 \leftarrow 13_0$	2882.19712(1)	$8_6 \leftarrow 9_6$	2880.92888(-2)
$13_6 \leftarrow 12_6$	2882.14963(1)	$8_0 \leftarrow 9_0$	2880.92390(7)
$13_0 \leftarrow 12_0$... ^a	$9_0 \leftarrow 10_0$	2880.86570(1)
$12_6 \leftarrow 11_6$	2882.09748(0)	$10_9 \leftarrow 11_9$	2880.8195(16) ^b
$12_0 \leftarrow 11_0$	2882.09324(1)	$10_0 \leftarrow 11_0$	2880.80664(3)
$11_0 \leftarrow 10_0$	2882.04075(0)	$11_6 \leftarrow 12_6$	2880.75131(1)
$10_6 \leftarrow 9_6$	2881.99233(1)	$11_0 \leftarrow 12_0$	2880.74539(-14) ^b
$10_0 \leftarrow 9_0$	2881.98822(3)	$12_9 \leftarrow 13_9$	2880.69807(13) ^b
$9_6 \leftarrow 8_6$	2881.93927(1)	$12_6 \leftarrow 13_6$	2880.69130(0)
$9_0 \leftarrow 8_0$	2881.93503(2)	$12_0 \leftarrow 13_0$	2880.68632(-6)
$8_0 \leftarrow 7_0$	2881.88110(-2)	$13_0 \leftarrow 14_0$	2880.62659(-2)
$7_0 \leftarrow 6_0$	2881.82777(3)	$14_6 \leftarrow 15_6$	2880.57068(1)
$6_0 \leftarrow 5_0$... ^a	$14_0 \leftarrow 15_0$	2880.56629(0)
$5_0 \leftarrow 4_0$	2881.71877(-2)	$15_9 \leftarrow 16_9$	2880.51487(-3)
		$15_6 \leftarrow 16_6$	2880.50961(-2)
		$15_0 \leftarrow 16_0$	2880.50565(1)
		$16_6 \leftarrow 17_6$	2880.44891(2)
		$16_0 \leftarrow 17_0$	2880.44350(-10) ^b
		$17_6 \leftarrow 18_6$	2880.38749(2)
		$17_0 \leftarrow 18_0$	2880.38315(0)
		$16_6 \leftarrow 19_6$	2880.32585(3)
		$18_0 \leftarrow 19_0$... ^a

^aPeaks obscured by strong overlapping Ar_2HCl , ArHCl or $(\text{HCl})_2$ lines.

^bPeaks are blended with Ar_2HCl transitions, and not used in the least squares fit.

Table 4.5 Spectroscopic constants (in cm^{-1}) determined from fits of the transition frequencies to symmetric top Hamiltonian. The $\nu_{\text{HCl}} = 0$ ground state values were fixed at values determined from microwave. The uncertainties in parentheses represent one standard deviation in the units of the last reported digit.

	$\text{Ar}_2\text{H}^{35}\text{Cl}$	
	$\nu_{\text{HCl}} = 0$	$\nu_{\text{HCl}} = 1$
B	0.028149387(3)	0.027997(2)
$D_J \times 10^8$	7.782(7)(23)	8.59(59)
$D_{JK} \times 10^8$	6.064(20)	10.12(28)
$\Delta(A-B) \times 10^4$		1.41(6) ^a
$\Delta D_K \times 10^8$		4.0(35) ^a
ν_0		2881.44217(2)

^a Due to the parallel nature of this band, only differences can be obtained.

complete assignment of the corresponding $\text{Ar}_3\text{H}^{37}\text{Cl}$ spectrum is not possible at the present S/N.

4.4 Discussion

The data obtained for Ar_2HCl and Ar_3HCl in the infrared region of the spectrum allow us to pursue an analysis of the vibrationally averaged geometries in the $\nu_{\text{HCl}} = 1$ manifold. However, the use of a geometric analysis need not imply a “rigid” structure; indeed, large amplitude motion of the HCl subunit is clearly indicated by the data. From the structural analysis of Ar_2HCl there are indications

already that nonpairwise additive forces are significant. The vibrational redshifts for Ar_nHCl ($n = 1-3$) clusters display much more of a linear dependence on n than in the analogous Ar_nHF complexes. Insight into these differences is provided by analysis of the Ar-HCl and Ar-HF pair potentials. Finally, theoretical investigation of the equilibrium structures and vibrational redshifts for larger clusters are performed to examine the size dependence.

4.4.1 Vibrationally averaged structures

The infrared cluster spectra for Ar_nHCl ($n = 1,2,3$) contain structural information on the ground and vibrationally excited states through the rotational constants, which are inversely proportional to the corresponding moments of inertia. The resulting structures necessarily represent vibrationally averaged geometries, and as a consequence of large amplitude motion of the HCl subunit can differ substantially from the equilibrium structures. This makes unambiguous interpretation of structural parameters more difficult, since for increasing number of Ar atoms there are far more large amplitude coordinates than rotational constants. Nevertheless, by fixing some of the more “rigid” internal degrees of freedom, vibrationally averaged structural parameters (based on an explicit model) can be extracted which prove instructive in probing intermolecular forces in these multibody systems.

The effect of HCl excitation on the Ar_nHCl vibrationally averaged geometry

can be determined from a comparison of the rotational constants in the ground and excited vibrational states. There are extensive microwave,²⁸⁻³⁰ far-,³¹⁻³⁶ and near-infrared^{26,37} spectroscopic measurements on Ar-HCl; a brief description of some of the changes in the vibrationally averaged ArHCl structure between the $\nu_{\text{HCl}} = 0$ and $\nu_{\text{HCl}} = 1$ vibrational manifolds is illustrative of trends observed in the higher Ar_nHCl clusters. In ArHCl there is a 0.93% decrease in the B value corresponding in a pseudodiatom approximation to a 0.47% increase (0.0186 Å) of R_{eff} , the distance between the HCl center of mass (com) and the Ar atom. This is somewhat unusual, since the monomer vibrational frequency red-shifts by 1.7667 cm^{-1} upon complexation with a single Ar atom, indicating a slight increase in the well depth in the $\nu_{\text{HCl}} = 1$ state. Indeed, much of the shift toward larger R_{eff} values in the $\nu_{\text{HCl}} = 1$ state can be accounted for by the anharmonic stretching of the HCl bond with one quantum of vibrational excitation which pushes the Ar out due to repulsive interactions with the hydrogen atom. Based on these results for ArHCl, one would therefore predict the analogous rotational constants in the larger Ar_nHCl clusters also to decrease due to a comparable increase in the Ar_n - HCl center of mass (com) separation.

A full inertial analysis of the actual equilibrium structure of Ar_2HCl necessarily must include vibrational averaging over large amplitude motion and requires information not contained in the near-IR rotational constants. Consequently, we invoke a more simplified approach, in which contributions from large amplitude

motion are absorbed into the rotational constants A , B , and C , which are then used to determine effective, vibrationally averaged center-of-mass separations between Ar-Ar (ρ_{eff}) and Ar₂ - HCl (R_{eff}). This requires an explicit model for the vibrationally averaged geometry of the cluster, which we take to be planar with the HCl pointing along the C_{2v} axis. This leads to the simple analytic expressions for R_{eff} and ρ_{eff} ,

$$R_{\text{eff}} = \sqrt{(P_A + I_{\text{HCl}}) / \mu} \quad (4.2a)$$

$$\rho_{\text{eff}} = \sqrt{2P_B / m_{\text{Ar}}} \quad (4.2b)$$

where P_A and P_B are the planar moments [e.g., $P_A = 1/2 (-I_A + I_B + I_C)$], I_{HCl} is the HCl moment of inertia, μ is the Ar_n - HCl reduced mass, and m_{Ar} is the Ar mass.

With these simple expressions we can attempt to interpret the small shifts both upon complexation and vibrational excitation of the monomer.

In the ground vibrational state, Eq. 4.2a leads to $R_{\text{eff}} = 3.4969$ and 3.4975 Å for Ar₂H³⁵Cl and Ar₂H³⁷Cl, respectively. The fact that the com separation is smaller for the ³⁵Cl isotope is consistent with the HCl oriented with the hydrogen atom pointing toward the Ar₂ com. For the $\nu_{\text{HCl}}=1$ vibrational state, R_{eff} increases by 0.0186 Å to 3.5155 and 3.5165 Å for Ar₂H³⁵Cl and Ar₂H³⁷Cl, respectively. This is in essentially perfect agreement with the shift in R_{eff} observed for ArHCl upon vibrational excitation of the HCl subunit. A somewhat different trend is seen in the

vibrationally averaged Ar – Ar distance. In the ground state ρ_{eff} is 3.8323 Å for $\text{Ar}_2\text{H}^{35}\text{Cl}$, whereas in the excited state this value is essentially unchanged, i.e., $\rho_{\text{eff}} = 3.8324$ Å. Thus, vibrational excitation of the HCl would appear to have almost no effect on the vibrationally averaged Ar – Ar separation, a trend that is echoed in both isotopes. This is at first glance quite surprising, since both the experimentally measured red-shifts of the Ar_nHCl clusters as well as the pairwise Ar – HCl potentials would predict a stronger attraction of each Ar atom to the HCl monomer upon vibrational excitation. This should “squeeze” the two Ar atoms closer together, and cause ρ_{eff} to decrease slightly. However, the triangular equilibrium geometry of the Ar_2HCl complex is at the optimum geometry for both Axilrod-Teller (triple dipole^{38,39}) and induced dipole-induced dipole repulsive three-body interactions, which would tend to increase the Ar-Ar separation. For Ar_2HCl , the competition between pairwise additive squeezing and repulsive three-body effects fortuitously cancel, which lead to essentially no change in Ar-Ar distance upon HCl vibrational excitation.

Further evidence in support of this interpretation can be found by comparison with the vibrationally averaged Ar-Ar separation in the bare Ar_2 dimer,^{40,41} $\rho_{\text{eff}} = 3.821(10)$ Å i.e., a considerable 0.011 Å shorter than in the Ar_2HCl trimer cluster. A similar estimate for the magnitude of these three-body effects on the Ar-Ar separation in Ar_2HCl can be made using the theoretical rotational constants reported by Cooper and Hutson,²³ calculated using both (i) the pairwise additive potential and

(ii) the pairwise additive potential modified with three-body terms due to Axilrod-Teller, induced dipole-induced dipole, and exchange quadrupole effects. Based on the vibrationally averaged inertial analysis embodied in Eq. 4.2, ρ_{eff} is predicted to increase by 0.028 Å from 3.810 to 3.838 Å when such three-body terms are included. Thus, the experimentally observed increase in ρ_{eff} from Ar₂ to Ar₂HCl, as well as the subsequent insensitivity of ρ_{eff} to HCl vibrational excitation is qualitatively consistent with modeling by Cooper and Hutson of three-body forces in Ar₂HCl.

Finally, we return briefly to the issue of vibrational averaging effects by examining the inertial defect, $\Delta=(I_C-I_A-I_B)$, which should vanish for a rigid planar structure. Furthermore, positive or negative values of the inertial defect reflect the degree of in-plane vs. out-of-plane large amplitude motion around a nominally planar geometry. The inertial defect in the $\nu_{\text{HCl}} = 1$ state for Ar₂H³⁵Cl is relatively large and positive ($\Delta= 4.006 \text{ amu } \text{Å}^2$), which would be consistent with significant in-plane zero-point vibrational motion of either the Ar₂ or HCl subunits. A positive contribution to the inertial defect by in-plane zero-point motion of the light H atom would be consistent with the “softer” in-plane (37.195 cm⁻¹) vs. out-of-plane (45.203 cm⁻¹) intermolecular frequencies measured in the ground HCl vibrational state.¹⁵⁻¹⁷ However, this H atom motion is not likely to be the dominant contribution, since the inertial defect is also positive even in the out-of-plane intermolecular excited state. This suggests that the inertial defect is dominated by in-plane zero-point motion of the heavy atom species, i.e., either the van der Waals stretch or bending/stretching

motion of the Ar₂ subunit. Similar trends have been noted in near-IR combination band studies of intermolecular modes in Ar₂HF and Ar₂DF clusters as well.¹⁹

The Ar₃HCl spectrum reflects parallel band excitation of a symmetric top, and as a result, there are a limited number of spectroscopic parameters from which to determine vibrationally averaged structural data. Furthermore, there are several additional torsional and bending vibrations of the Ar₃ subunit which may further complicate the influence of vibrational averaging on the rotational constants. Nevertheless, if we model Ar₃-HCl as a pseudodiatom, with the Ar₃ plane perpendicular to a C_{3v} Ar₃-HCl axis, then we can solve for the vibrationally averaged separation between the com of the Ar₃ and HCl subunits from the *B* rotational constant. From the values in Table 4.5, calculations indicate that *R*_{eff} increases by +0.54% from 3.299 Å in the ground vibrational state to 3.317 Å in the *v*_{HCl} = 1 excited state i.e., increasing consistently by the same 0.018 Å that is observed in both Ar-HCl and Ar₂-HCl complexes. Similar quantitative data on the change in the Ar-Ar distance *ρ*_{eff} are not easily available, since there is no information in a parallel band on the *A* rotational constant. However, the data do constrain Δ(*A* – *B*), which, with the experimentally measured value of Δ*B*, determined Δ*A* to be quite small [–1.1(6)×10^{–5} cm^{–1}]. Based on theoretical predictions of *C* = 0.02907 cm^{–1} for the Ar₃ trimer, this would imply that *ρ*_{eff} in Ar₃-HCl does not change by more than a few parts in 10⁴ upon vibrational excitation. This again would be consistent with the comparable insensitivity to HCl monomer vibrational excitation observed in both

Ar₂HCl isotopomers, and attributed previously to a delicate balance between (i) squeezing of the Ar-Ar bonds due to site competition for the HCl and (ii) increased three-body Ar₃ repulsion in the vibrationally excited state.

4.4.2 Predicted Ar_nHCl equilibrium structures

In the Ar_nHF and Ar_nDF series, pairwise additive potentials constructed from the well studied Ar-HF and Ar-Ar potentials proved quite useful in characterizing the equilibrium structures of the various cluster sizes. Similarly, we have constructed pairwise additive potentials for Ar_nHCl based on (i) the H6(4,3,0) ArHCl potential of Hutson³ and (ii) the HFD-B Ar-Ar potential of Aziz *et al.*²² which allows the equilibrium structure and binding energy for clusters to be calculated as a function of n . Specifically, we use the approximate pairwise additive potential for Ar_nHCl combined with a quasi-Newton algorithm to search for local and global minima on the full potential surface. In the following section we restrict the discussion to relatively small clusters ($n = 1-4$) representative of the range experimentally observed. However, later we will return to predictions for much larger clusters more characteristic of the bulk matrix phase.

The lowest energy structures for $n = 1,2,3$, are qualitatively identical to the structures determined for Ar_nHF. The symmetries of equilibrium structures of Ar₂HCl (C_{2v}) and Ar₃HCl (C_{3v}) are also consistent with the number of equivalent Ar

atoms determined from the nuclear spin statistics present in the spectra of these clusters. For Ar_nHCl ($n = 1,2,3$) the next higher minima are calculated to be 28, 57, and 133 cm^{-1} higher in energy. For both ArHCl and Ar_2HCl the next higher energy “isomer” is obtained by a rotation of the HCl monomer by 180° to form the ArClH and Ar_2ClH structures, respectively. Experimental information on these “isomers” has been obtained by infrared excitation of the Σ bend in ArHCl (23.6572 cm^{-1}) and in Ar_2HCl (39.5547 cm^{-1}). The predictive power of such a simple classical analysis is encouraging and suggests it is worth while to pursue the same approach to predict the structures of still larger Ar_nHCl structures.

The global minimum for Ar_4HCl is a structure with C_{2v} symmetry with a binding energy of $-1.087.9 \text{ cm}^{-1}$. The next higher minimum (C_{3v}) is only 19.0 cm^{-1} higher in energy, but the two minima are separated by a barrier of approximately 100 cm^{-1} . This is qualitatively different than both predicted and observed in Ar_4HF , where the C_{3v} isomer appears to be the true global minimum and the C_{2v} isomer minimum is theoretically predicted to be 15.43 cm^{-1} higher in energy.⁴²

Interestingly, we have not been able to observe the corresponding C_{3v} $n = 4$ cluster spectrum in Ar_nHCl , even though we currently detect the Ar_3HCl cluster with even higher S/N than in the previous Ar_3HF studies. If the C_{2v} structure in fact survives as a global minimum after zero-point effects are included, this may partially be due to a lack of a strongly overlapped Q -branch predicted for the perfectly symmetric C_{3v} structure, which for low concentrations presents a far more readily sharp feature in a

congested spectrum. Such differences between Ar_4HCl and Ar_4HF underscore the subtle balance of forces that takes place in finite size clusters, whereby small changes in the pairwise interactions can be responsible for shifts in the energy ordering of isomers, and thus influence the predominant structures of clusters observed under supersonic jet conditions.

4.4.3 Vibrational redshifts

Another window into the size dependent effects of sequential solvation of HCl in Ar afforded by near infrared studies is the red-shift of the high frequency HCl stretch upon complex formation. As in $\text{Ar}_n\text{HF/DF}$ there exists a rigorous methodology for calculating the size dependence of the HCl vibrational red-shift in the Ar_nHCl system. Specifically, by taking advantage of the well known Ar-HCl and Ar-Ar pair potentials, the intermolecular wave functions can be rigorously calculated on both the $\nu_{\text{HCl}} = 0$ and $\nu_{\text{HCl}} = 1$ adiabatic potentials; the difference in the ground state energies on these two potentials is equal to the red-shift induced by complexation. There are only two approximations in this procedure, (i) the adiabatic separability of the high frequency HCl stretch vibration from the low frequency intermolecular motion, and (ii) the assumption of perfect pairwise additivity in the potential surface. The first approximation has proven to be quite valid in both ArHF and ArHCl ; consequently, the magnitude of the second pairwise additive

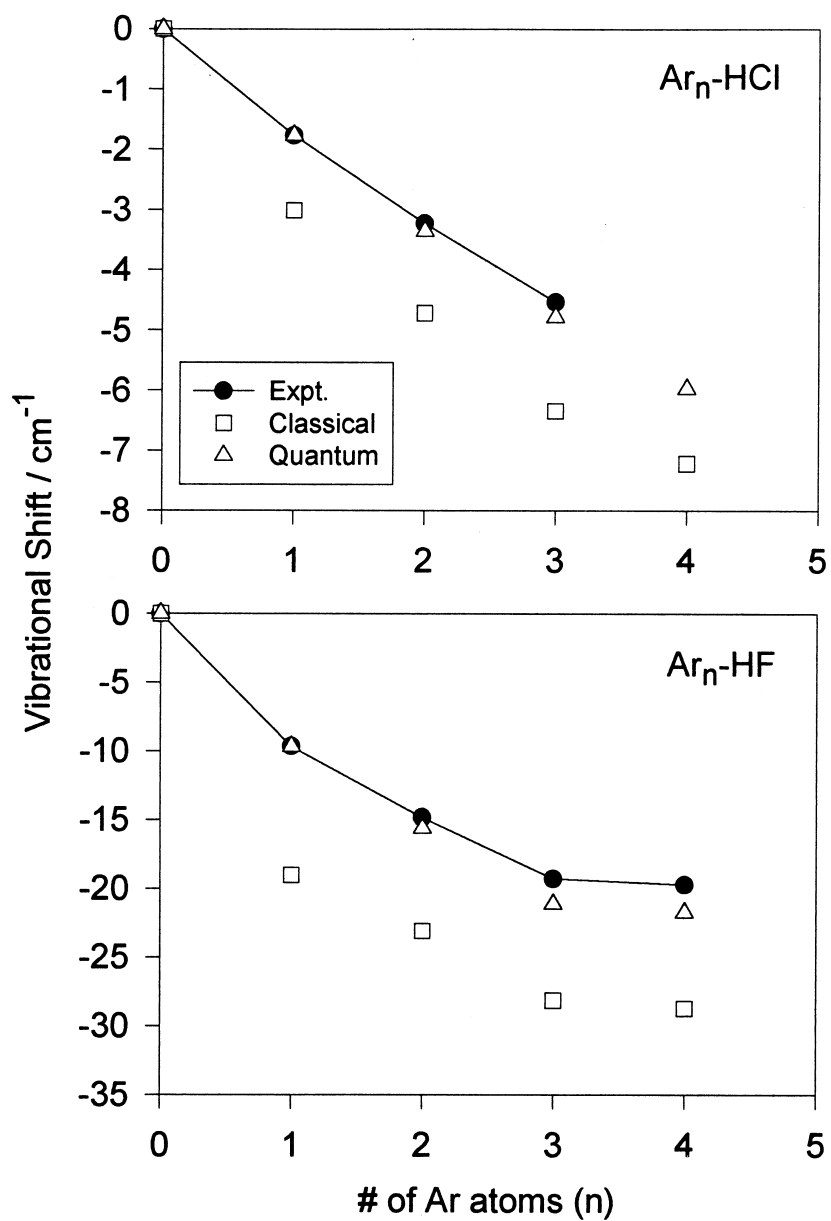


Figure 4.3 The experimental HX vibrational shifts for (upper) Ar_nHCl and (lower) Ar_nHF as a function of n . Also included are the calculated shifts from (i) classical calculations and (ii) quantum variational and Monte Carlo calculations (Refs. 49,47,46)

approximation can be tested by comparison with experiment. The experimental red-shifts are plotted in Figure 4.3, for both Ar_nHCl and Ar_nHF , and the Ar_nHCl values are reported in Table 4.6.

In order to obtain some preliminary information about the size dependence of the HCl vibrational red-shifts in Ar_nHCl clusters based on the pairwise additive potential, we resort to a simple approximation where the red-shift in Ar_nHCl is modeled by the change in the absolute well depth (D_e) of the potential caused by vibrational excitation of the HCl from $\nu_{\text{HCl}} = 0$ to $\nu_{\text{HCl}} = 1$. Though purely classical, this method has the advantage of simplicity, can be applied to arbitrarily sized clusters, and therefore provides useful qualitative insight into the relationship

Table 4.6. Experimental HCl vibrational origins and the corresponding red-shifts for Ar_nHCl ($n = 1-4$) clusters. Included are red-shifts calculated using the approximate classical method and variational^a ($n = 1$) and Quantum Monte Carlo^b ($n = 2-4$) techniques. The experimental matrix shift^c is also included for comparison.

	Origin	Red-shift	Classical	Quantum
HCl	2885.9754			
ArHCl	2884.2087	-1.7667	-3.012	-1.765 ^a
Ar ₂ HCl	2882.7518	-3.2236	-4.717	-3.35(7) ^b
Ar ₃ HCl	2881.4422	-4.5332	-6.343	-4.78(7) ^b
Ar ₄ HCl	-7.215	-5.97(14) ^b
Ar matrix	2870.80 ^c	-15.18		

^a Reference 3

^b Reference 47

^c Reference 25

between HCl vibrational red-shift and the size/geometry of the complex. As we will later show, it also permits intriguing contrast with similar classical studies of larger Ar_n - HF clusters by Bacic *et al.*⁴³

As seen in Figure 4.3, such classical calculations for HF/HCl vibrational red-shifts do not quantitatively reproduce the high resolution experimental results. Specifically, these calculations (see Figure 4.3) consistently overestimate the red-shift for $n = 1-4$ clusters, by an amount which is nearly constant at $\approx 9-11 \text{ cm}^{-1}$ and $\approx 1.5-2.0 \text{ cm}^{-1}$ for HF and HCl clusters, respectively. Conversely, 5D quantum variational^{42,44,45} and/or full diffusion quantum Monte Carlo^{46,47} calculations have been performed for the Ar_nHF clusters (see Figure 4.3), which are in nearly quantitative agreement with experiment. The source of this much larger shift between classical and quantum predictions is readily interpreted in the terms of a HF vibrational dependence to intermolecular zero-point energy, which must therefore increase by $\approx 9-11 \text{ cm}^{-1}$ in the $\nu_{\text{HF}} = 1$ state. This hypothesis can of course be explicitly verified for the $n = 1$ ArHF cluster where all intermolecular vibrations have been spectroscopically observed, and quantum calculations on the $\text{H}(6,3,2)$ potential indicate a $\approx 9.4 \text{ cm}^{-1}$ increase in the zero-point energy between $\nu_{\text{HF}} = 0$ and $\nu_{\text{HF}} = 1$ intramolecular excitation. Somewhat more surprising is that this increase in zero-point energy appears to be relatively insensitive to the number of Ar atoms from $n = 1$ to 4. However, this would be consistent with a simple picture that these shifts are dominated by HX bending and Ar_n - HX van der Waals stretch modes. From a

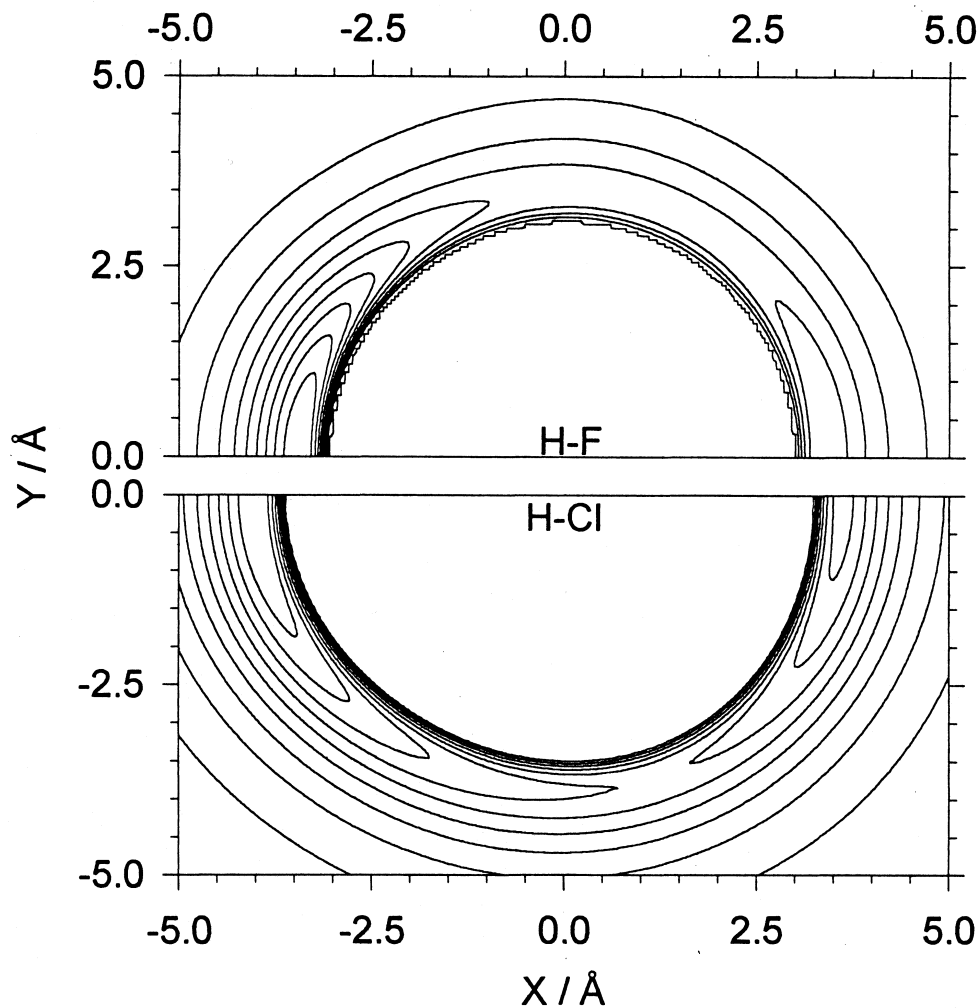


Figure 4.4 Contour plots of the H6(4,3,2) Ar-HF (upper) and H6(4,3,0) Ar-HCl (lower) intermolecular potentials in Cartesian coordinates with the HX center-of-mass placed at the origin and the H-atom pointing in the negative x-direction. In each plot there are 10 equally spaced contours indicating the bound ($E < 0 \text{ cm}^{-1}$) region of the potential. Notice that the global minimum of the Ar-HF potential is at a smaller distance from the origin and note the greater angular anisotropy of the Ar-HF potential.

similar line of argument, the consistent overestimation of redshifts in the corresponding Ar_nHCl complexes indicate that the zero-point energy increases by $\approx 1.5 - 2.0 \text{ cm}^{-1}$ in the $\nu_{\text{HCl}} = 1$ state.

The availability of vibrational redshift data on both Ar_nHCl and Ar_nHF clusters permit a direct comparison of “solvation” effects in these two systems. First of all, both series of complexes display a monotonic increase in the red-shift as Ar atoms are added sequentially. This largely reflects the vibrational state dependent change in the corresponding dimer potentials. Specifically, the binding energies in the $\nu_{\text{HX}} = 1$ vs $\nu_{\text{HX}} = 0$ state increase by 3.0 cm^{-1} and 19.0 cm^{-1} , respectively, for Ar-HCl and Ar-HF , thus redshifting the HX vibrational frequency upon complex formation. As predicted from a simple pairwise additive model, this redshift monotonically increases with number of Ar atoms, though the magnitude of these incremental red-shifts is clearly sensitive to (i) differences in the ν_{HX} - dependent Ar-HF vs Ar-HCl pair potentials, (ii) the vibrationally averaged locations of the additional Ar atoms, as well as (iii) more subtle nonpairwise additive interactions.

The different incremental redshifts for Ar_nHCl and Ar_nHF can be understood from an examination of the two Ar-HX pair potentials. In the case of $\text{Ar}_n - \text{HF}$, the first Ar produces by far the largest incremental red-shift ($\approx 10 \text{ cm}^{-1}$), with progressively weaker red-shifts for additional Ar atoms. By way of contrast, the red-shift for the first Ar atom in Ar-HCl is much smaller ($\approx 2 \text{ cm}^{-1}$) and much more nearly constant per additional atom. The incremental redshift behavior in Ar-HF has

been explained as due to a combination of angular “competition” of the Ar atoms for the linear global minimum geometry, and the significant angular anisotropy of Ar-HF $v_{\text{HX}} = 1$ and 0 potentials. This differs qualitatively from the nearly linear redshifts observed and predicted in Ar_nCO_2 , where there are multiple nearly isoenergetic T-shaped binding sites for the initial several Ar atoms.⁴⁸ Examination of the Ar-HF and Ar-HCl potentials in Figure 4.4 illustrates qualitatively why the Ar_nHCl incremental red-shift is nearly constant. First of all, the angular anisotropy of the Ar-HCl potential is significantly less “focused” at the linear configuration than is the case for Ar-HF. Secondly, the Ar-HCl potential minima occur at larger values of R than for Ar-HF, so that more than one Ar atom can sample the HCl well region without being energetically penalized by strong Ar-Ar repulsion. This combination of effects make the binding of successive Ar atoms to HCl much more “equivalent” than for Ar_nHF and thus resulting is a more linear dependence of the red-shift on n .

Finally, we can eliminate the zero-point contributions to the red-shift for small clusters of Ar_nHCl by comparison with diffusion Quantum Monte Carlo calculations by Lewerenz.⁴⁹ These calculations are based on the same pairwise additive potential surfaces used in the classical calculations; the ground state energy differences obtained for clusters with $v_{\text{HCl}} = 1$ and 0 correspond to the pairwise additive redshifts predicted in the corresponding cluster. The results, shown in Figure 4.3 and included in Table 4.6, indicate a greatly improved but still not perfect agreement with the experimental redshifts. In particular, the predicted redshifts for

the trimer and tetramer are larger by $\approx 5\%$ than experimentally observed, which is consistent with similar trends observed in Ar_nHF and Ar_nDF clusters. Based on the quantitative success of the Ar-HCl surface in reproducing high resolution near and far-IR spectroscopic observations, the residual discrepancies are therefore almost certainly due to neglect of three-body interactions in the pairwise additive surface and, as in $\text{Ar}_n\text{HF/DF}$ clusters, may be used for further rigorous tests of non-pairwise additive force models.

4.4.4 Extrapolation to matrix isolation studies

An implicit goal in the study of finite size clusters is to obtain sufficiently accurate multidimensional intermolecular potentials (both pairwise and nonpairwise) in order to permit realistic predictive models of condensed phase behavior to be constructed. Specifically, the present work provides a direct connection with bulk phase FTIR studies of HCl in cryogenic Ar matrices.^{24,25} Though the level of detail provided by such matrix isolation studies is limited by lower resolution in the condensed phase, comparisons can nevertheless be made at the level of HCl vibrational redshifts as a function of the surrounding Ar environment. With this goal in mind, we have used the simple pairwise additive Ar_nHCl potential discussed in Sec. 4.4.2 to obtain minimum energy structures for $n \leq 55$ Ar atoms. Furthermore, since the Ar-HCl potential is parameterized as a function of ν_{HCl} , the vibrational red-

shift for this structure can be estimated from the $\nu_{\text{HCl}} = 1 \leftarrow 0$ energy difference for a given minimum energy structure for a given number of Ar atoms. Though the simplicity of this classical model neglects zero-point motion as well as three-body (and higher order) interactions among the subunits, it does offer the corresponding advantage of consistency of method for clusters large enough to approximate behavior under bulk conditions. Specifically, the results reported here correspond to up to 4 “solvent shells” ($n \leq 54$), which, though not impossible to model theoretically with diffusion Quantum Monte Carlo methods, would make rigorous calculations of the redshifts and vibrationally averaged structures exceedingly difficult.

This question is addressed as follows. Computational studies of the Ar_nHCl with $n = 1 - 12$ have been performed to establish trends in the equilibrium structures near the global minima for each cluster size (see Figure 4.5). Interestingly, though $n = 12$ corresponds to the first shell occupancy for an octahedral site in a fcc matrix, this does not necessarily imply that the lowest energy structure is HCl fully solvated by Ar atoms. Indeed, for Ar_nHCl clusters from $n = 1$ to 12, the lowest energy structural motif reflects build up of a solvation “cap” localized around the H-atom end of HCl. Though there are numerous higher-lying local minima for the larger clusters, the structures in Figure 4.5 reflect global minima, which do not require significant reorganization of the first shell from Ar_nHCl to $\text{Ar}_{n+1}\text{HCl}$. Of course, there are also local minima corresponding to “fully solvated” cluster geometries for $n \approx 12$, but the model predicts these to be $\approx 149 \text{ cm}^{-1}$ *higher* than the energetically

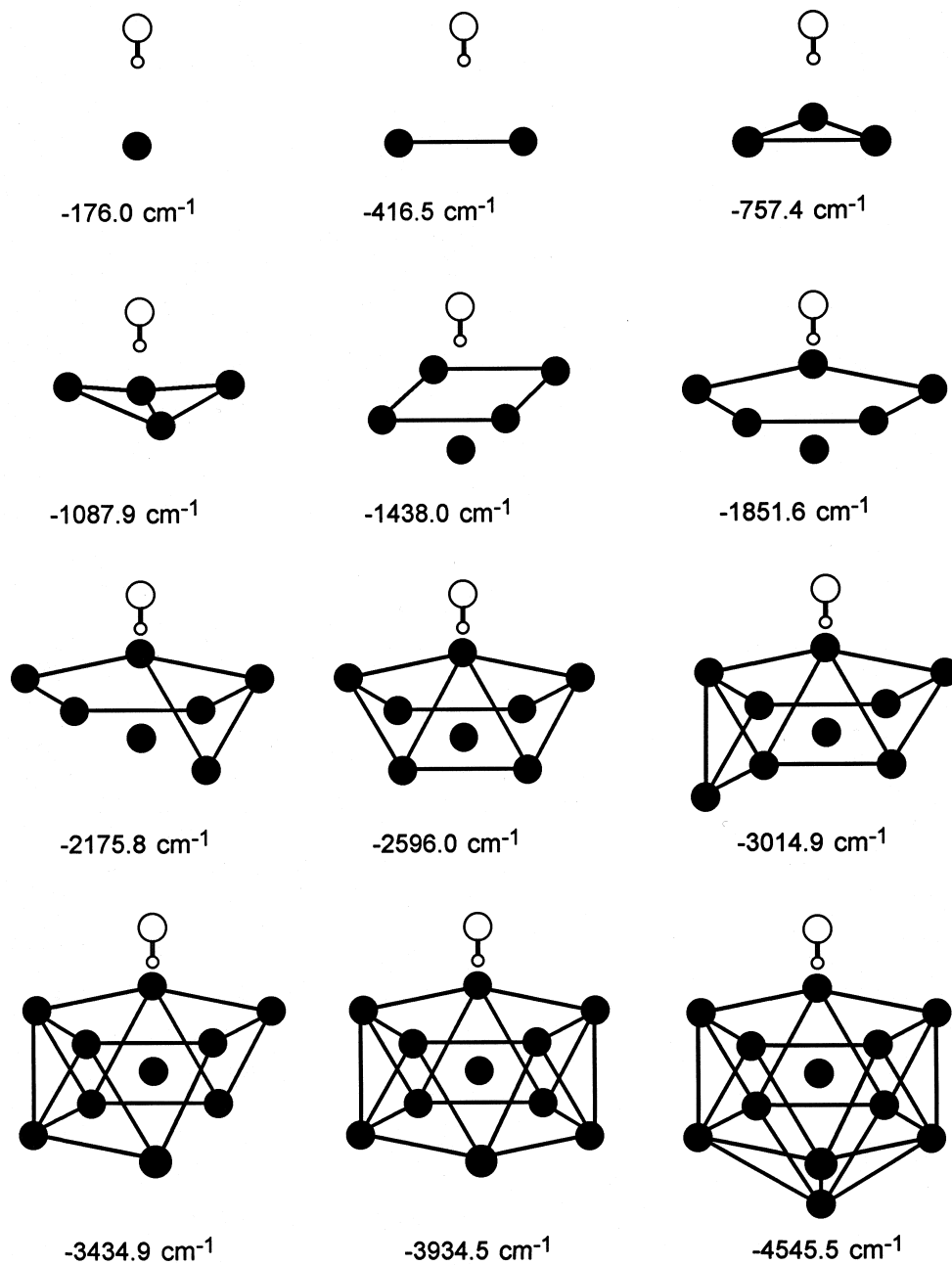


Figure 4.5 Pictorial representations of the minimum energy structures for the Ar_nHCl ($n=1-12$) series. The numbers under each structure are the binding energies in cm^{-1} .

more stable “partially solvated” geometries. The key point of these results is that the pairwise additive potentials predict that HCl prefers to form “surface” vs “interior” sites in a finite size Ar cluster.

It is worth noting that this is qualitatively different from the behavior previously found by Bacic *et al.* in Ar₁₂HF cluster,⁴³ where the fully solvated geometry is $> 40 \text{ cm}^{-1}$ lower in energy than any partially solvated isomeric geometries. This is clearly demonstrated in Figure 4.6, which indicated the local structural minima and corresponding energies for both interior and surface adsorbed HCl and HF in an Ar₁₂ cluster. This is not due simply to a competition between the energetics of the two pairwise binding potentials, which are relatively close ($D_e = -220.2 \text{ cm}^{-1}$ and -176.0 cm^{-1} for ArHF and ArHCl) and both substantially in excess of the Ar-Ar binding energy ($D_e = 99.5 \text{ cm}^{-1}$). What appears to be more important is the larger van der Waals “size” of the HCl vs HF in the matrix (i.e. see Figure 4.4), and thus the significant distortion of the Ar matrix upon substitution of a HCl vs HF subunit. In essence, the HCl molecule is too big to be solvated in the middle of the Ar₁₂ cluster; instead, the energetically more favorable configuration is with the HCl on the surface where the Ar atoms can adopt the bare Ar₁₂ minimum energy structure. This emphasizes the delicate balance between the Ar-Ar and Ar-HCl intermolecular forces present in these clusters. In addition, it highlights the difficulty in extrapolating structural results for small clusters, which are dominated by Ar-HCl interactions, to the bulk where structure is dominated by the many Ar-Ar

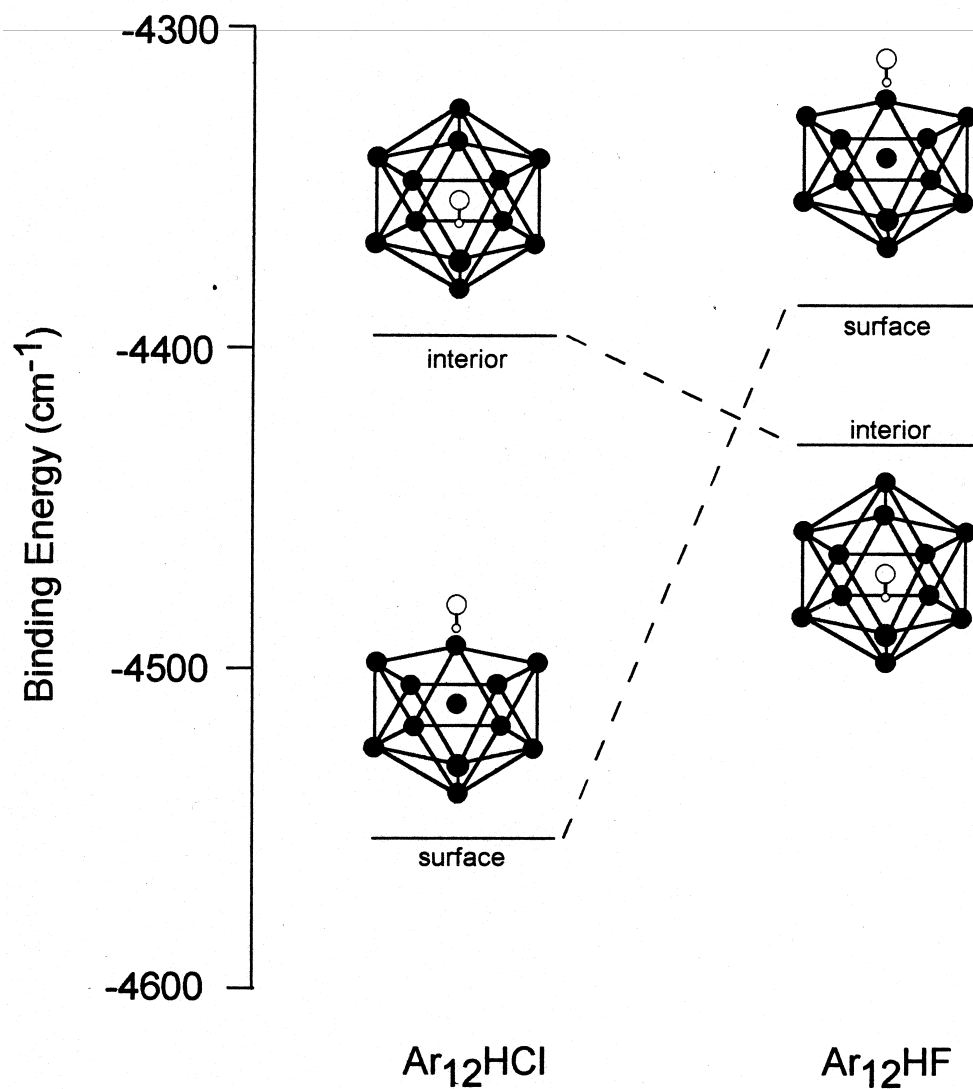


Figure 4.6 Plot of the calculated binding energies for surface and interior HX ($\text{X}=\text{Cl}, \text{F}$) sites in an Ar_{12} cluster. Note that the HCl prefers a surface site while the HF adopts a fully solvated geometry.

interactions.

In a typical experimental preparation of an Ar/HCl matrix, the HCl is trapped in an interior site by coadsorption of the Ar/HCl gas mixture and which for an annealed Ar crystal would correspond to a single substitution site in a fcc lattice. Consequently, in order to best compare red-shifts predicted from the Ar_nHCl pairwise additive potential with those of the matrix, local energetic minima for finite Ar_nHCl clusters have been obtained as a function of the number of solvation shells, n_{shell} , the minimization procedure is started with the HCl molecule substituted for a single Ar atom symmetrically in the center of a perfect fcc lattice. Local minimization of the first fcc solvation shell ($n_{\text{Ar}} = 12$) collapses to the icosahedral structure discussed previously, but this is still higher in energy than the “surface site” HCl. Also worth noting is that this slight energetic preference for an icosahedral vs fcc lattice structure at the first solvation shell level is quickly shifted with additional solven shells. For $n_{\text{Ar}} = 18$, the six additional nearest neighbors “squeeze” the first solvation shell to form a minimum energy structure that is much closer to a perfect fcc lattice. Though it is always difficult to identify a given structure unambiguously as a global vs local energetic minimum on such a multidimensional potential, all structures determined from different starting structures (e.g. icosahedral) result in higher energy structures. Energy minimization for the next two solvation shell structures ($n_{\text{Ar}}=42$ and $n_{\text{Ar}}=54$) starting from a perfect fcc lattice serves to stabilize this incipient fcc structure further into place, as indeed expected in the limit of the.

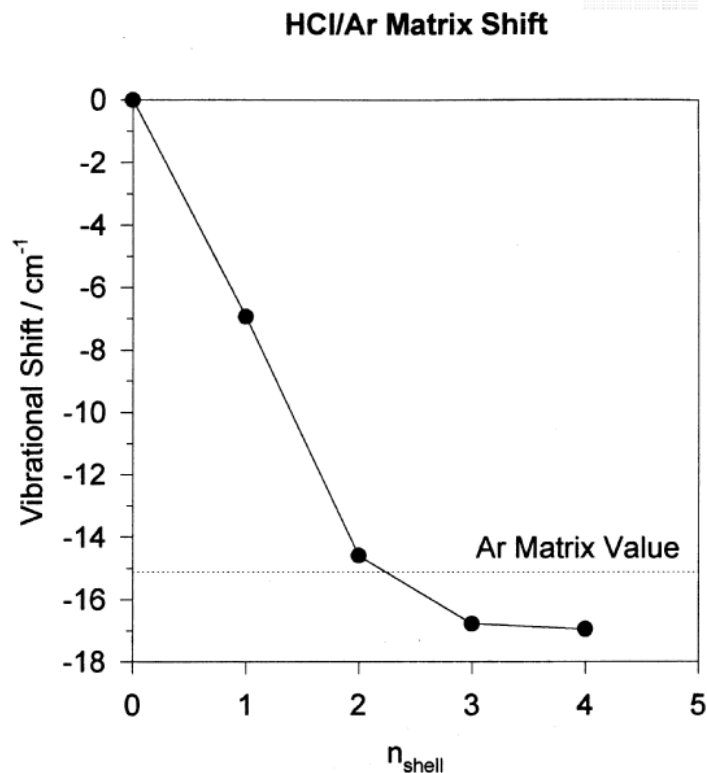


Figure 4.7 Calculated HCl vibrational shift as a function of the number of fcc solvation shells. The dashed line indicates the experimental Ar matrix value.

bulk matrix. It is important to note that these structures are fully relaxed, and to the best of our knowledge represent the unstrained, local minimum energies for HCl surrounded by a specific number of solvation shells

With the procedure reasonably converged for obtaining the local fcc lattice structures around the HCl subunit, it makes sense to look at the vibrational red-shifts as a function of solvation shell number. The results for the first four solvation shells are reported in Figure 4.7, and indicate several interesting points. First of all, the HCl vibrational red-shift for the first solvent shell is $\approx 6.9 \text{ cm}^{-1}$, which is less than

half of the 15.18 cm^{-1} red-shift observed in matrix isolation studies. This is qualitatively different from what had been previously noted in similar theoretical studies of Ar_nHF clusters,⁴³ where the first solvent shell had already achieved a red-shift (44.70 cm^{-1}) within 10% of the experimental matrix results. As a necessary corollary, the red-shifts predicted for HCl continue to grow significantly beyond the first solvation shell, reaching an asymptotic value only after closure of the third or fourth shell. Stated in simple physical terms, the HCl chromophore “feels” the environment of the Ar lattice well beyond its nearest neighbors, in clear contrast to the behavior inferred for HF in matrices. Of course, this effect must eventually saturate with the number of solvation shells; by $n_{\text{shell}} = 4$, the predicted red-shift of $\approx 17\text{ cm}^{-1}$ for Ar_nHCl is in qualitatively good agreement with the experimental matrix result of 15.18 cm^{-1} .

More quantitatively, however, the results of these classical red-shift calculations for sequential solvation of HCl by Ar clearly overshoot the matrix value by $\approx 1.8\text{ cm}^{-1}$. Though only 10% of the total red-shift, this discrepancy is quite similar to the trend established for small Ar_nHCl ($n = 1,2,3$) clusters, which also overestimate the experimental red-shifts by $\approx 1.5\text{ cm}^{-1}$. From comparison of predicted with experimental red-shifts in Figure 4.3, these appear to be a nearly constant offset for both HCl and HF clusters and due predominantly to neglect of zeropoint motion and three-body interactions in these calculations. Indeed, if we take the red-shift discrepancy for the largest cluster ($n = 3$) as an approximate

measure of this error, the corrected prediction for the HCl red-shift in an Ar matrix would be $\approx 15.2 \text{ cm}^{-1}$, i.e., in essentially quantitative agreement with the 15.18 cm^{-1} experimental result.

4.5 Summary

High-resolution, rotationally resolved spectra of the $\nu_{\text{HCl}} = 1 \leftarrow 0$ stretch in Ar_2HCl and Ar_3HCl have been recorded using a slit-jet infrared spectrometer. For both clusters the Ar atoms are distributed symmetrically about the HCl axis, on the H-atom side of the HCl. Near-infrared excitation of the Ar_nHCl complexes slightly increases the vibrationally averaged Ar_n - HCl center of mass separation, but the magnitude of these changes is insignificant compared with the large amplitude motion present in these clusters. Structural analysis of the Ar_2HCl trimer does show evidence for nonpairwise intermolecular forces, and the magnitude of structural changes are consistent with previous theoretical work on three-body repulsion in Ar_nHCl . At least for the complexes studied experimentally, the sequential growth of Ar around the HCl chromophore is identical to the analogous Ar_nHF ($n=1-3$) complexes due to the similarities in the Ar-HX potentials.

The vibrational frequency of the HCl monotonically shifts to the red with sequential addition of Ar atoms but does not display the strong nonlinearity measured in Ar_nHF ($n=1-4$). This difference in the behavior of the sequential red-

shift reflects the less anisotropic nature of the angular-radial Ar-HCl potential. Quantum calculations of the vibrational red-shift in the Ar_nHCl are needed to quantify the magnitude of nonpairwise additive contributions. We have also investigated the size evolution of the equilibrium structures and approximate HCl vibrational red-shifts for Ar_nHCl clusters ($n = 1-12$) utilizing the accurate pairwise additive Ar_nHCl potential. These studies indicate qualitative structural differences for Ar_{12}HCl and Ar_{12}HF surrounded by one solvation shell. Specifically, for Ar_{12}HCl , the lowest energy structure consists of HCl bound to the *surface* of an Ar_{12} cluster, as opposed to the *interior* minimum energy structure predicted for Ar_{12}HF .

The availability of matrix isolation spectra for HCl is argon also makes comparison between experiment and theory possible for the condensed phase. These calculations indicate the HCl red-shift is sensitive to Ar atoms well beyond its 12 nearest neighbors in the first solvation shell, but is reasonable converged by $n_{\text{shell}} \approx 4$. By way of contrast, the red-shifts in the Ar_nHF system are mostly sensitive only to Ar atoms in direct contact with the HF chromophore, thus suggesting that a more local description of the condensed phase interactions should suffice. This work demonstrates clearly that the combination of high resolution spectroscopy of gas phase clusters with classical and/or quantum theoretical analysis on accurate pair potentials offers an interesting alternative window into solvent shell dynamics in the condensed phase environment.

As a final comment, since the completion of this work early on in my

graduate career, full 5D quantum variational calculations on $\nu_{\text{HCl}}=1 \leftarrow 0$ vibrational red-shifts ($\approx 3.07 - 3.18 \text{ cm}^{-1}$) in Ar_2HCl have been reported by Ernesti and Hutson⁵⁰ that are in reasonably good agreement with experiment (3.2236 cm^{-1}). Furthermore, their work correctly predicts a red-shift that is *decreased* from the pairwise additive results (3.329 cm^{-1}) by nonpairwise additivity in the potentials, though by roughly twofold more than experimentally observed.

References for Chapter 4

- 1 M. A. Suhm and D. J. Nesbitt, *Chemical Society Reviews* **24**, 45 (1995).
- 2 D. J. Nesbitt, *Chemical Reviews* **88**, 843 (1988).
- 3 J. H. Hutson, *Journal of Physical Chemistry* **96**, 4237 (1992).
- 4 J. M. Hutson, *Journal of Chemical Physics* **96**, 6752 (1992).
- 5 R. J. Le Roy and J. M. Hutson, *Journal of Chemical Physics* **86**, 837 (1987).
- 6 R. Cohen, C. and R. J. Saykally, *Journal of Chemical Physics* **98**, 6007 (1993).
- 7 C. A. Schmuttenmaer, R. C. Cohen, and R. J. Saykally, *Journal of Chemical Physics* **101**, 146 (1994).
- 8 H. S. Gutowsky, T. D. Klots, C. Chuang, J. D. Keen, C. A. Schuttenmaer, and T. Emilsson, *Journal of the American Chemical Society* **107**, 7174 (1985).
- 9 H. S. Gutowsky, T. D. Klots, C. Chuang, C. A. Schmuttenmaer, and T. Emilsson, *Journal of Chemical Physics* **83**, 4817 (1985).
- 10 H. S. Gutowsky, T. D. Klots, C. Chuang, C. A. Schmuttenmaer, and T. Emilsson, *Journal of Chemical Physics* **86**, 569 (1987).
- 11 H. S. Gutowsky, T. D. Klots, C. Chuang, J. D. Keen, C. A. Schmuttenmaer, and T. Emilsson, *Journal of the American Chemical Society* **109**, 5633 (1987).
- 12 H. S. Gutowsky, C. Chuang, T. D. Klots, T. Emilsson, R. S. Ruoff, and K. R. Krause, *Journal of Chemical Physics* **88**, 2919 (1988).
- 13 T. D. Klots and e. al., *Journal of Chemical Physics* **87**, 5315 (1987).
- 14 T. D. Klots and e. al., *Journal of Chemical Physics* **87**, 4383 (1987).

- 15 M. J. Elrod, D. W. Steyert, and R. J. Saykally, *Journal of Chemical Forces* **94**, 58 (1991).
- 16 M. J. Elrod, S. D. W., and R. J. Saykally, *Journal of Chemical Physics* **95**, 3182 (1991).
- 17 M. J. Elrod, J. G. Loeser, and R. J. Saykally, *Journal of Chemical Physics* **98**, 5352 (1993).
- 18 M. J. Elrod, D. W. Steyert, and R. J. Saykally, *Molecular Physics* **81**, 579 (1994).
- 19 J. T. Farrell and D. J. Nesbitt, *Journal of Chemical Physics* (1996).
- 20 A. McIlroy, R. Lascola, C. M. Lovejoy, and D. J. Nesbitt, *Journal of Physical Chemistry* **95** (1991).
- 21 J. T. Farrell, Jr., S. Davis, and D. J. Nesbitt, *Journal of Chemical Physics* **103**, 2395 (1995).
- 22 R. A. Aziz, *Journal of Chemical Physics* **99**, 4518 (1993).
- 23 A. Cooper and J. Hutson, *Journal of Chemical Physics* **98**, 5337 (1993).
- 24 D. E. Mann, N. Acquita, and D. White, *Journal of Chemical Physics* **44**, 3453 (1966).
- 25 L. Young and C. B. Moore, *Journal of Chemical Physics* **98**, 5337 (1984).
- 26 B. J. Howard and A. S. Pine, *Chemical Physics Letters* **122**, 1 (1985).
- 27 J. K. G. Watson, *Journal of Chemical Physics* **46**, 1935 (1967).
- 28 S. E. Novick and e. al., *Journal of Chemical Physics* **65**, 1114 (1976).
- 29 S. E. Novick, P. Davies, S. J. Harris, and W. Klemperer, *Journal of Chemical Physics* **59**, 2273 (1973).
- 30 J. M. Hutson and B. J. Howard, *Journal of Chemical Physics* **74**, 6520 (1981).

- 31 K. L. Busarow and e. al., *Chemical Physics Letters* **141**, 289 (1987).
- 32 M. D. Marshall and et al., *Journal of Chemical Physics* **83**, 4924 (1985).
- 33 D. Ray and et al., *Journal of Chemical Physics* **84**, 1171 (1986).
- 34 R. L. Robinson, D. Ray, D.-H. Gwo, and R. J. Saykally, *Journal of Chemical Physics* **87**, 5149 (1987).
- 35 R. L. Robinson, D. H. Gwo, and R. J. Saykally, *Journal of Chemical Physics* **86**, 5211 (1987).
- 36 R. L. Robinson, D. H. Gwo, and R. J. Saykally, *Journal of Chemical Physics* **87**, 5156 (1987).
- 37 C. M. Lovejoy and D. J. Nesbitt, *Chemical Physics Letters* **146**, 582 (1988).
- 38 Y. Muto, *Proceedings of the Physical Society of Japan* **17**, 629 (1943).
- 39 B. M. Axilrod and E. Teller, *Journal of Chemical Physics* **11**, 299 (1943).
- 40 E. A. Colbourn and A. E. Douglass, *Journal of Chemical Physics* **65**, 1741 (1976).
- 41 P. R. Herman, P. E. Laroque, and B. P. Stoicheff, *Journal of Chemical Physics* **89**, 4535 (1988).
- 42 S. Liu, Z. Bacic, J. W. Moskowitz, and K. E. Schmidt, *Journal of Chemical Physics* **100**, 7166 (1994).
- 43 S. Liu, B. Zlatko, J. W. Moskowitz, and R. E. Schmidt, *Journal of Chemical Physics* **103**, 1829 (1993).
- 44 S. Liu and e. al., *Journal of Chemical Physics* **101**, 6359 (1994).
- 45 S. Liu, Z. Bacic, and J. W. Moskowitz, *Journal of Chemical Physics* **101**, 10 (1994).
- 46 P. Niyaz, Z. Bacic, J. W. Moskowitz, and R. E. Schmidt, *Chemical Physics Letters* **252**, 23 (1996).

- 47 M. Lewerenz, *Journal of Chemical Physics* **104**, 1028 (1996).
- 48 J. M. Sperhac, M. J. Weida, and D. J. Nesbitt, *Journal of Chemical Physics* (1996).
- 49 M. Lewerenz, (private communication).
- 50 A. Ernesti and J. M. Hutson, *Journal of Chemical Physics* **106**, 6288 (1997).